stellarator news

Published by Fusion Energy Division, Oak Ridge National Laboratory
Building 5700 P.O. Box 2008 Oak Ridge, TN 37831-6169, USA

Editor: James A. Rome Issue 108 April 2007
E-Mail: jar@ornl.gov Phone (865) 482-5643
On the Web at *http://www.ornl.gov/sci/fed/stelnews*

Steady-state experiment using ICRF heating in LHD

Steady-state operation is a key issue for fusion research. Long-pulse discharges have been carried out in some tokamak devices using lower-hybrid current drive. A feature of stellarators is that no plasma current is necessary to confine the plasma. This makes it advantageous to operate stellarators in steady state; any steady-state heating method can be used to achieve long-pulse operation.

The Large Helical Device (LHD) is located in Toki, Japan. Because LHD has superconducting helical windings, it has the potential for steady-state operation [1], and one of the main research aims of the LHD experiment is to demonstrate the ability to sustain the plasma for a long time. Heating in the ion cyclotron range of frequencies (ICRF) has technical advantages for high-power and steady-state operation compared to the existing electron cyclotron heating (ECH) or neutral beam injection (NBI) heating systems in LHD. Thus, ICRF heating has been mainly used for most steady-state experiments in LHD.

Fig. 1. The LHD ICRF antennas.

The ICRF antennas are installed in the upper and lower ports and located on the outboard side of the torus, as shown in Fig. 1. Upper and lower antenna pairs are located on two toroidal sections, at the 3.5 and 7.5 ports. There is also an antenna pair at the 4.5 port as a reserve. The antenna is movable in the radial direction by 15 cm. The antenna current strap and the Faraday shield are water-cooled. The inside of the inner conductor and the outside of the outer conductor of the transmission line are also water-cooled.

Temperatures of the ICRF antenna were monitored using an IR camera. The antenna temperature increases by more than 100ºC at an ICRF power of 250 kW and a pulse length of 5 s using an antenna-plasma gap of 7 cm; these

In this issue . . .

are the parameters used in the earlier short-pulse and long-pulse ICRF heating experiments. The increase in temperature declines dramatically when the antenna moves away from the plasma. It is reduced to 10ºC when the antenna-plasma gap is 12 cm. The plasma loading resistance also decreases but remains at 3 Ω at that antenna position. The antenna position was set to an antenna-plasma gap of 12 cm beginning with the 8th cycle of experiments in fiscal year (FY) 2004. A liquid stub tuner, which was developed for the steady state operation, is used for the impedance matching circuit [2].

Real-time impedance matching was applied during injection of ICRF power. The reflected power increased gradually during long-pulse ICRF operation without impedance feedback control. The net injected ICRF power decreased and a reflection interlock terminated the RF pulse when the ratio of the reflected power to the forward power exceeded 20%. The increased reflected power was suppressed to less than 1% of the forward power using feedback control of the liquid surface level during long-pulse operation.

Four RF transmitters can be operated simultaneously in steady state. Their operation tests were performed using a steady-state dummy load at a power of 0.5 MW with a pulse length of 30 min or 1 h, and at a power of 0.25 MW with a pulse length of 1 h for each transmitter. Each of the transmitters is connected to four loop antennas. Minority heating was selected for the ICRF heating scheme. This was found to be optimum for the short-pulse ICRF heating experiments [3]. The positions of the ion cyclotron resonance layers are shown in Fig. 2.

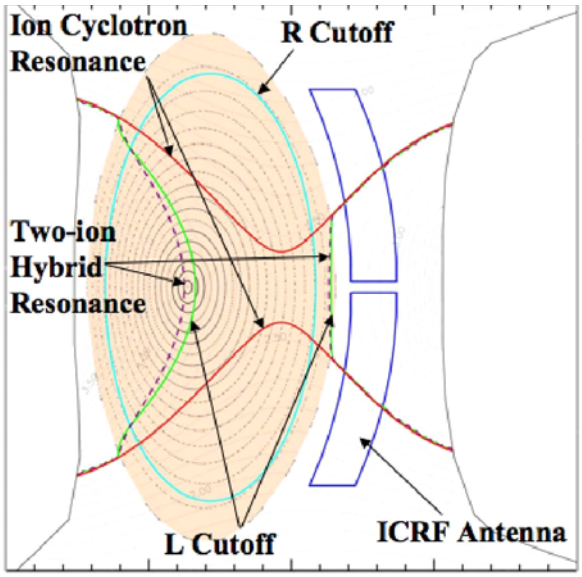

Fig. 2. Positions of the resonance and cut-off layers in a poloidal plasma cross section at the antenna location. The ion cyclotron resonance layer is located near the saddle point of the magnetic field.

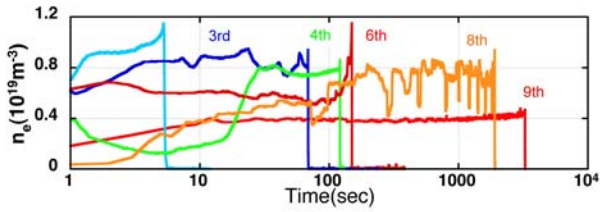

Fig. 3. Traces of line-averaged electron density of the longest discharge in each experimental campaign. These are equivalent to the maximum discharge length. Labels such as 3rd mean experimental campaigns. The 3rd experimental campaign occurred in FY 1999 and the 9th was in FY 2005.

The center of the major radius is on the left side. A helium plasma with minority hydrogen ions was used in the experiment. The central electron density is 1.0×10^{19} m^{-3} and the minority ratio is 10% in this calculation. The wave frequency is 38.47 MHz, the magnetic axis position is 3.6 m, and the magnetic field on axis is 2.75 T. Power is expected to be absorbed by the hydrogen ions around and between the two ion cyclotron resonance layers.

ICRF heating experiments have been successfully carried out in LHD [3,4] as shown in Fig. 3. Heating experiments started using a short pulse for a few seconds. Thereafter, the pulse length was extended as LHD and the ICRF system were improved for steady-state operation [5]. The discharge length reached 150 s in the 6th experimental campaign of FY 2002. The plasma duration time was limited by an uncontrollable increase in density. An increase in the H_α signal as compared with other species was notable before the plasma collapse. It was thought that the hydrogen influx was caused by out-gassing from carbon in divertor plates and antenna side protectors. Some of the divertor graphite plates were then replaced by superior ones [6]. The maximum allowable heat flux for the new plates is four times higher, and their outgassing ratio is less than one-third of that observed with the old plates. The plasma discharge time was extended to more than 1000 s with the new operational method described below.

In plasma experiments, sweeping the magnetic axis position is an important technique. Figure 4 is a comparison of the case with a fixed magnetic axis and one with magnetic axis sweep. When the magnetic axis is fixed at 3.55 m, the temperature of the divertor plate continues to increase as shown at the bottom of the left -hand side of Fig.4. The position of the divertor plate, which is located in the upper part of the port 3I, is identified as “3I-U” in Fig. 4. The temperature exceeds 300ºC in 180 s and has a tendency to increase further. When the magnetic axis is swept, the temperature rise of the 3I-U plate is reduced at the outward axis position, as shown on the right-hand side of Fig. 4. The position of the magnetic axis is shown at lower right.

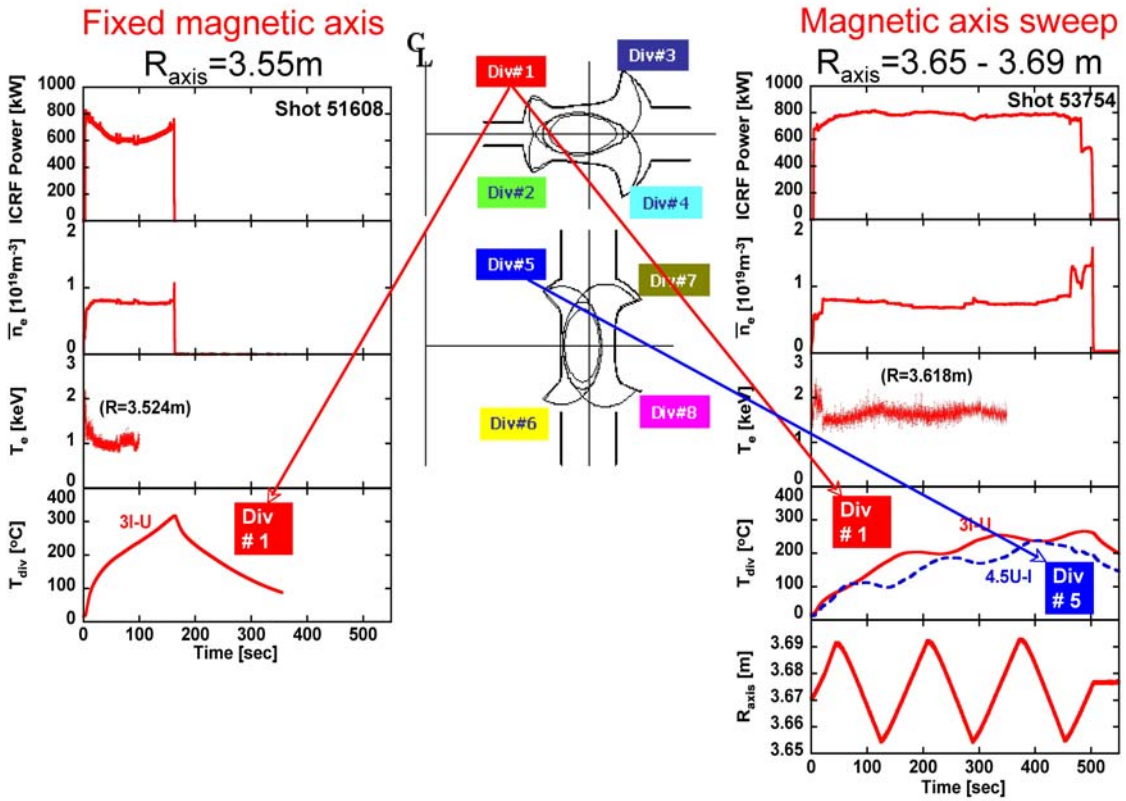

Fig. 4. Evolution of plasma parameters in the case of a fixed magnetic axis (left) and magnetic axis sweep (right). The ICRF power, line-averaged electron density, electron temperature, temperature of the divertor plate, and the position of the magnetic axis are shown. The positions of divertor plates at poloidal cross section are also indicated (center).

The temperature rise of the other divertor plate, 4.5U-I (inner part of port 4.5U), shows an inverse trend. The heat load at the divertor plate is then scattered by the magnetic axis sweep [7]. The plasma discharge continues for 500 s, and the temperature of the divertor plate remains below 280ºC during the discharge.

A plasma discharge of more than 3000 s (50 min) was achieved through integration of the improved systems and operating techniques such as mentioned above [8]. The time history of the plasma parameters of the longest discharge is shown in Fig. 5. The duration of the plasma discharge time is 3268 s (54 min, 28 s.) The plasma was sustained mainly by ICRF power of 0.38 MW on average. ECH power of approximately 110 kW was also used to support the discharge. The total injected heating energy reached 1.6 GJ. This is the highest input energy injected into any plasma fusion experimental device so far. The line-averaged electron density was about 0.4×10^{19} m^{-3}, and the central ion temperature was about 1 keV. The electron density was controlled to maintain a constant value by helium gas-puffing feedback. The position of the magnetic axis was swept between 3.64 m and 3.67 m. The measured divertor temperature was less than 300ºC. This is within the tolerance level. However, the maximum temperature at the antenna feedthrough reached about 80ºC at the end of the discharge and was not saturated. Stronger cooling is needed for the ceramic part of the antenna feedthrough.

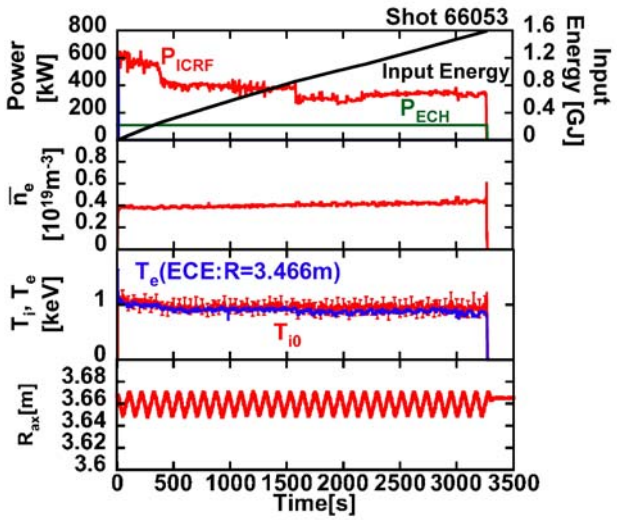

Fig. 5. Time history of plasma parameters for the longest discharge obtained so far. The heating power, total input energy, line-averaged electron density, ion and electron temperatures, and position of the magnetic axis are plotted.

The plasma discharge was terminated suddenly and uncontrollably. At the end of the discharge, the intensity of the Fe X signal increased rapidly without a precursor. This event was followed by a rise in the electron density and radiation loss power and a decrease in the electron temperature. This indicates that iron impurities flowed into the plasma. Abnormal termination often occurs due to sparks, which are observed on a real-time plasma monitor viewing the inside of the vacuum vessel. The sparks may be caused by high-energy ions generated by ICRF heating. During a discharge, spark occurrences are monitored using a CCD camera. In the 54-min discharge, the ICRF power was manually controlled. The power was reduced when sparks occurred and was (rarely) increased to maintain the plasma. The inside of the vacuum vessel was inspected after the experimental campaign, and no damage caused by the sparks was observed.

Figure 6 shows the injected heating energies versus plasma duration time for steady-state experiments. Both LHD results and tokamak results are shown. The input energy of 1.6 GJ is the world record thus far in fusion plasma experimental devices. In LHD, a discharge more than one hour long was achieved using ECH (lower red point). In those experiments, the heating power was low and the density and temperature of the plasma were also low. Higher power operation is necessary for the next phase of steady-state experiments. Conquest of the plasma termination problem caused by the influx of metallic impurities is most important for higher power and longer-pulse operation of LHD.

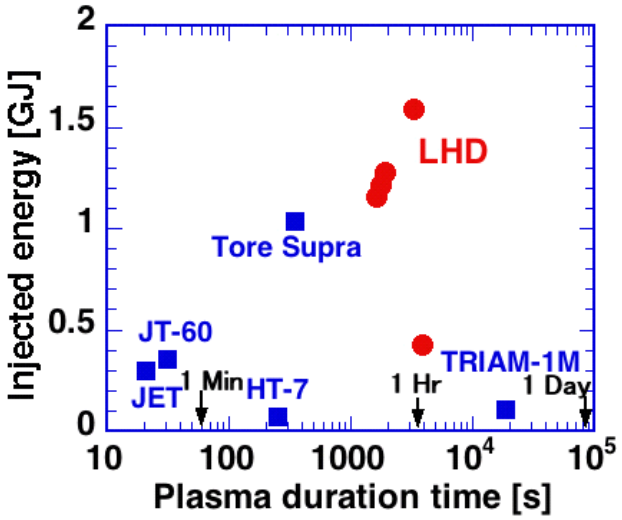

Fig. 6. Injected energy and plasma duration time achieved by fusion experimental devices.

Tetsuo Seki for LHD experimental group
National Institute for Fusion Science
E-mail: seki@nifs.ac.jp
Telephone: +81-572-58-2193

References

[1] O. Motojima et al., Nucl. Fusion **43** (2003) 1674.
[2] K. Saito et al., Rev. Sci. Instrum. **72** (2001) 2105.
[3] K. Saito et al., Nucl. Fusion **41** (2001) 1021.
[4] T. Seki et al., J. Plasma Fusion Res. **5** (2002) 478.
[5] R. Kumazawa et al., Nucl. Fusion **46** (2006) S13.
[6] Y. Kubota et al., Fusion Eng. Des. **75** (2005) 297.
[7] S. Masuzaki et al., Nucl. Fusion **42** (2002) 750.
[8] T. Mutoh et al., in Proc. IAEA Fusion Energy Conference 2006 (16–21 Oct. 2006, Chengdu, China), EX/P1-14.

Nonlocal transport and fast pulse propagation

Perturbative experiments provide valuable time-dependent transport information in a relatively controlled setting that can be used to validate and test transport models. In these experiments, the transient response of the plasma to externally applied small perturbations, e.g., plasma edge cooling and heating power modulation, is followed in time; see for example Refs. [1,2] and references therein. In the case of cold pulses, it has been observed that perturbations travel from the edge to the core at speeds significantly greater than the typical diffusive time scales, raising doubts about the validity of models based on the standard diffusion paradigm [3–5]. Here we discuss the use of nonlocal transport models as an alternative to diffusive models in the description of these phenomena. Understanding nonlocal transport is particularly relevant for stellarators, in which it has been observed that nonlocal dependences on the flux are needed to consistently describe fast transient responses in transport experiments including W7-AS [6], TJ-II [7], and LHD [8].

We will limit attention to the problem of radial transport of a single scalar field. The starting point is the conservation law,

$$\partial_t T = -\partial_x q + S, \tag{1}$$

where T is the transported scalar (e.g., temperature), x is a normalized radial coordinate, S is the source, and q is the flux which contains all the dynamic information of the transport processes. The main goal of transport modeling is to find a relation between q and T to close Eq. (1). In the standard diffusive model, a local relation of the form

$$q_d = -\chi_d \partial_x T \tag{2}$$

is assumed and the problem is reduced to finding the function χ_d, which in general can depend on x, t, T, and the gradients of T. This local description assumes the existence of a well-defined transport scale and that no significant interactions of widely separated regions of the plasma occur. As a result, these models tend to underestimate the speed of propagation of cold pulses.

Nonlocality is believed to play an important role in non-diffusive plasma transport in general and in the fast propagation of pulses in particular [5]. Within the standard diffusive transport model, some level of nonlocality can be incorporated through nontrivial nonlinear dependences of the effective diffusivity on the transported fields and their gradients. However, here we explore a more direct approach based on the use of transport operators that replace the local flux-gradient relation in Eq. (2) with a nonlocal relation in which the flux at a given point can in principle depend on the global properties of the temperature profile. The generic form of this type of nonlocal models is

$$q(x) = -\chi \partial_x \int K(x-y) T(y) \mathrm{d}y \tag{3}$$

where the function $K(x–y)$ accounts for the non-local contribution of the temperature at point y to the flux at point x. The decay of the function K measures the degree of nonlocality. As expected, in the case of a Dirac delta function, $K = \delta(x-y)$, the local diffusive model is recovered. The type of non-local model is determined by the specific form of the function K. Here, following [9] we consider algebraic decaying function of the form $K \sim 1/(x-y)^{(\alpha-1)}$, and write the non-local flux as

$$q_{\mathrm{nl}}(x,t) = -\chi_{\mathrm{nl}} \partial_x \left[l \int_a^x \frac{T(y,t)}{(x-y)^{\alpha-1}} dy + r \int_x^b \frac{T(y,t)}{(y-x)^{\alpha-1}} dy \right], \tag{4}$$

where $1 < \alpha < 2$, l and r are constant, and χ_{nl} is the nonlocal diffusivity. The first term on the right hand side of Eq. (4) represents the nonlocal contribution of the flux at x from the plasma located between the core at a and point x, whereas the second term on the right-hand side of Eq. (4) represents the contribution from the plasma between x and the edge at b. The relative weight of these two terms is determined by the parameters
$l = -0.5(1-\theta)/\cos(\alpha\pi/2)$ and
$r = -0.5(1+\theta)/\cos(\alpha\pi/2)$ with $-1 < \theta < 1$. For $\theta = 0$, transport is symmetric because $l = r$. In the extremal case $\theta = -1$ ($\theta = 1$), only the "core side" ("edge side") of the plasma contributes to nonlocal transport.

In principle one could use a different function $K(x–y)$ to define the nonlocal operator. However, there are strong physical, analytical, and computational reasons to choose algebraic decaying functions. In Fourier space, Eq. (4) takes the form

$$\hat{q}_{\mathrm{nl}} = -\chi_{\mathrm{nl}} [l(-ik)^{\alpha-1} - r(ik)^{\alpha-1}] \hat{T}(k),$$

where the carets designate the Fourier transform of the variable. As expected, in the limit $\alpha = 2$ and $l = r$, q_{nl} reduces to the local flux in Eq. (2). The limit $\alpha \to 1$ is less trivial, but it can be shown [9] that in this case Eq. (4) reduces to the nonlocal flux for Landau fluid closures [10]. Thus, depending on the value of α, the proposed non-local flux interpolates between the local diffusive flux and a free streaming flux. For general α, the scaling $\hat{q}_{\mathrm{nl}} \sim k^{\alpha-1}$ motivates the interpretation of the operator on the right-hand side of Eq. (4) as a fractional derivative of order $\alpha - 1$, i.e., $q_{\mathrm{nl}} \sim \partial_x^{\alpha-1} T$ [11]. There is also a very appealing interpretation of Eq. (4) in the context of statistical

mechanics. In particular, it can be shown that the fractional diffusion transport equation resulting from substituting Eq. (4) into Eq. (1) is the fluid or continuum limit of a self-similar, non-Brownian random walk without a characteristic transport scale (see for example Ref. [9] and references therein). This motivates the use of the nonlocal model in Eq. (4) to describe scale-free, self-similar turbulent transport in plasmas as discussed in Refs. [13,14] for the case of resistive pressure-gradient driven turbulence. It has also been shown that quasilinear-type renormalization calculations of turbulent transport that avoid the restrictive localization hypothesis lead to fractional diffusion equations [15]. From the computational point of view, the definition of the flux in terms of fractional derivatives allows the implementation of efficient, accurate, and stable finite difference numerical methods [16, 9], which can eventually be incorporated in predictive transport codes to account for nonlocality.

In a previous publication [9] we showed that the fractional transport model describes some of the basic nondiffusive transport phenomenology of fusion plasmas, including the anomalous scaling of the confinement time τ with system size L, $\tau \sim L^{\alpha}$; profile peaking with off-axis fueling; pinch effects; and fast propagation phenomena. Continuing this work, we present here preliminary results of a systematic study of the role of nonlocality in the shape and propagation speed of cold pulses. The results are based on the numerical integration of Eq. (1), where the flux $q = q_{\rm d} + q_{\rm nl}$ includes the diffusive local channel in Eq. (2) and the nonlocal transport channel defined in Eq. (4). We consider a finite-size domain $x \in (a, b)$, where $a = 0$ denotes the magnetic axis and $b = 1$ the plasma edge in normalized radial coordinates. The boundary conditions are zero total flux at the magnetic axis, $q_{\rm d}(0) + q_{\rm nl}(0) = 0$, and constant temperature at the edge, $T(1) = 0$. Consideration of a finite-size domain with boundary conditions requires the regularization of the fractional derivative operators in Eq. (4); for details on the regularization and a description of the numerical method, see Ref. [6]. We assume a constant Gaussian diffusivity $\chi_{\rm d}$ and a nonlocal diffusivity of the form

$$\chi_{\rm nl} = \chi_s\{1 + \tanh[(x - x_0)/\lambda]\} - \chi_{\rm nl}(0)$$

with $\chi_s = 1$ $x_0 = 0.1$, and $\lambda = 0.025$. Thus, near the core, $x \sim 0$, $\chi_{\rm nl} \ll 1$, and transport is dominated by diffusion, whereas outside the core, for $x > x_0$, nonlocal effects become important and transport is nondiffusive. In the pulse propagation studies, a steady-state temperature profile $T_0(x)$ was first computed by integrating the transport model with an on-axis source. A pulse perturbation with a Gaussian profile centered at $x = 0.75$ was introduced at $t = 0.01$ and the perturbed temperature
$\tilde{T}(x, t) = T(x, t) - T_0(x)$ and perturbed flux
$\tilde{q}(x, t) = q(x, t) - q_0(x)$ were followed in time.

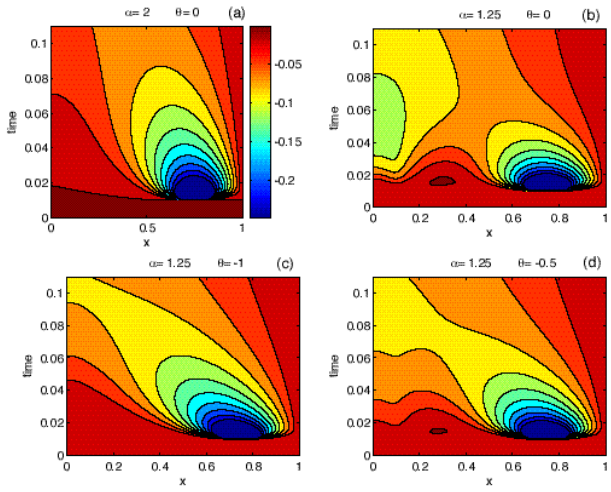

Fig.1. Contour plot of the spatio-temporal evolution of the normalized temperature perturbation following the introduction at $t = 0.01$ of a cold pulse centered at $x = 0.75$. For reference, panel (a) shows the pure diffusive transport case ($q_{\rm nl} = 0$). Panels (b), (c) an (d) show the dynamics including both the diffusive flux in Eq. (2) and the nonlocal fractional flux in Eq. (4) for (b) $\alpha = 1.25$ and $\theta = 0$ (symmetric case), (c) $\theta = -1$ (extremal case,) and (d) $\theta = -0.5$ (asymmetric case).

Figure 1 shows the spatio-temporal evolution of the normalized temperature perturbation $\tilde{T}$. For reference, Fig. 1(a) shows the pure diffusive case in the absence of nonlocality, i.e., for $q_{\rm nl} = 0$. As expected, in this case the pulse spreads on a diffusive time scale and the effect of the perturbation at the core is negligible. Figures 1(b), 1(c), and 1(d) show the results for $\alpha = 1.25$ and $\theta = 0$, -1, and -0.5 respectively. In case (b) the nonlocality of the fractional flux gives rise to a very fast, large response at the core, as evidenced by the large green blob shown in Fig. 1(b) around $t \sim 0.05$ and $x \sim 0$. Cases (c) and (d) correspond to asymmetric fluxes. As discussed in Ref. [9], in these cases the asymmetry gives rise to a inward pinch. The effect of the pinch is evident in the tilting of the pulse observed in Fig. 1(c) which corresponds to the extremal case $\theta = -1$. However, the presence of the pinch is accompanied by a fast decay of the nonlocal tail linking the core which eventually leads to a weaker response in the core, compared to the symmetric case.

Figure 2 shows the spatio-temporal evolution of the perturbed flux $\tilde{q}$ corresponding to $\tilde{T}$ in Fig. 1. As before, Fig. 2(a) shows the diffusive case. The strong nonlocal effect already noted in Fig. 1(b) is also seen in Fig. 2(b), where the pulse perturbation gives rise to positive flux perturbation that rapidly spreads to the core and cools the plasma. The spreading is weaker in the extremal and intermediate cases, Figs. 2(c) and 2(d). The almost instantaneous appearance of a finite flux in the fractional case near

the core where the local gradient of the temperature vanishes is a direct manifestation of the nonlocality of the process.

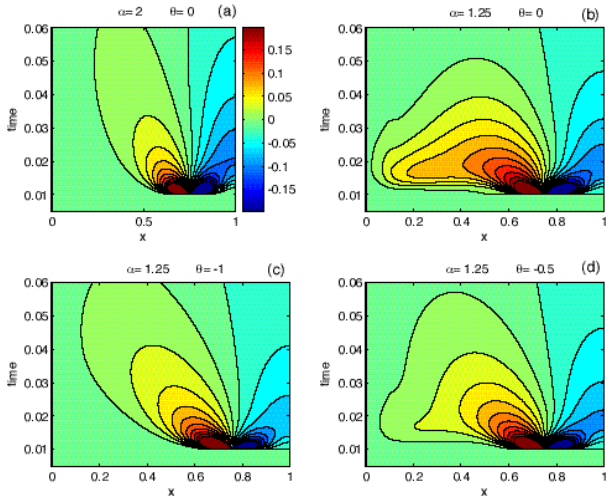

Fig. 2. Contour plot of the spatio-temporal evolution of the normalized total flux perturbation corresponding to the temperature evolution in Fig.1.

Figure 3 shows the temperature traces of the normalized temperature perturbation in Fig. 1. The plots display the temperature evolution as a function of time at different spatial locations for the cases $(\alpha,\theta) = (2,0)$, $(1.25,0)$, $(1.25,-1)$, and $(1.25,-.5)$. As expected, in the vicinity of the pulse the dynamics is dominated by the local diffusive response and there is little deviation among the four cases considered. Moving away from the location of the pulse towards the core, there is a crossover behavior on the speed of the signal depending on the asymmetry. As a result of the fractional pinch, for $0.3 \le x \le 0.6$ the signal corresponding to the asymmetric extremal case $\theta = -1$ (green curve) exhibits the fastest propagation. However, as discussed before the inward pinch is accompanied by a weakening of the left tail of the pulse, and near the core the signal corresponding to the symmetric $\theta = 0$ case (red curve) exhibits faster propagation. The propagation speed in the symmetric fractional case is about ten times larger than the propagation speed in the diffusive case (black curve). The plots in Fig. 3 qualitatively resemble the temperature time traces typically observed in perturbative cold pulse experiments in tokamaks and stellarators.

Summarizing, in this article we have studied the role of nonlocal transport on fast pulse propagation phenomena. The results are based on a fractional transport model that incorporates nonlocality directly through an integral operator. Fractional models are a natural generalization of diffusive models, and they have been successfully applied in the past to describe non-diffusive transport in fusion plasmas and tracers' transport in plasma turbulence. The nonlocality introduced by the fractional operator yields a pulse propagation speed ten times as large as the diffusive propagation speed for $\chi_s = \chi_d = 1$. Depending on the asymmetry of the nonlocal operator, a pinch effect can speed up the pulse for short distances. However, at long distances, nonlocal effects dominate the propagation speed of the pulse. Numerical results not shown here indicate that the propagation velocity of the pulse increases when the "stiffness level" χ_s/χ_d increases. In particular, for $\chi_s = 5$ and $\chi_d = 1$, the nonlocal pulse propagation speed can be up to 20 times larger than the diffusive speed. Future work will focus on the application of the fractional model to perturbative transport experiments involving heat modulation.

An interesting open problem is the modeling of temperature reversal perturbative experiments. As observed in tokamaks and more recently in stellarators [17], in these experiments a cold pulse perturbation at the edge can give rise to nonlocal prompt heating of the core. Preliminary studies indicate that fractional diffusion can exhibit similar phenomenology. Further work on this challenging problem will be discussed in a future publication.

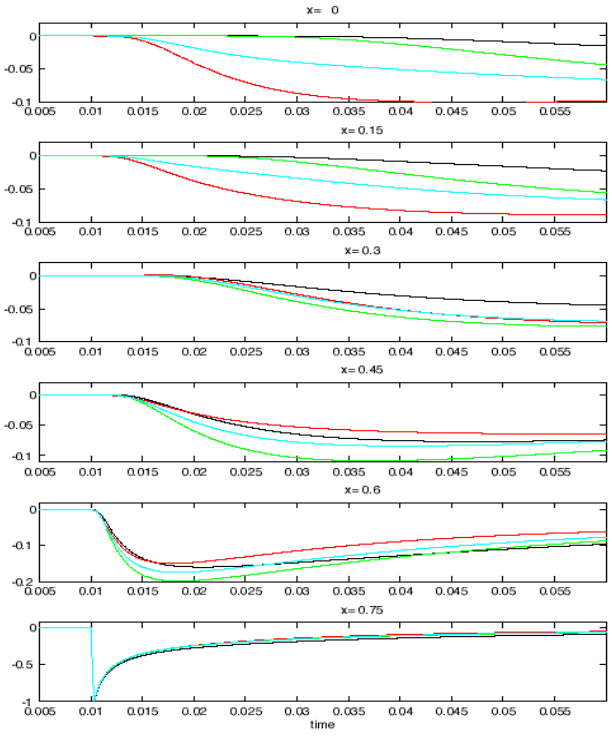

Fig. 3. Traces of the normalized temperature perturbation at various spatial locations. The plot at the bottom gives the time evolution at the location where the pulse was introduced. The plot at the top gives the response at the core. The colored curves correspond to the four cases in Figs. 1 and 2, with the diffusive case $(\alpha,\theta) = (2,0)$ shown in black, the fractional symmetric case$(\alpha,\theta) = (1,25,0)$ shown in red, the fractional extremal case $(\alpha,\theta) = (1,25,-1)$ in green, and the fractional asymmetric case $(\alpha,\theta) = (1,25,-0.5)$ in cyan.

Acknowledgments

Research supported by the U.S. Department of Energy under contract DE-AC05-00OR22725.

Diego del-Castillo-Negrete
Fusion Energy Division
Oak Ridge National Laboratory
Oak Ridge, TN 37830, USA
E-mail: delcastillod@ornl.gov

References

[1] N. Lopez Cardozo, Plasma Phys. Control. Fusion **37**, 799 (1995).

[2] P. Mantica and F. Ryter, C.R. Phys. **7**, 634–649 (2007).

[3] K.W. Gentle et al., Phys. Plasmas **2**, 2292 (1995).

[4] P. Mantica et al., in Proc. 19th Int. Conf. Fusion Energy, Lyon, 2002 [IAEA, Vienna, 2002], EX/P1-04.

[5] J.D. Callen and M.W. Kissick, Plasma Phys. Controlled Fusion **39**, B173 (1997).

[6] U. Stroth et al, Plasma Phys. Control. Fusion,**38**, 611 (1996).

[7] B.P. van Milligen, E. de la Luna, et al., Nucl. Fusion **42,** 787 (2002).

[8] S. Inagaki et al., Nucl. Fusion **46,** 133 (2006).

[9] D. del-Castillo-Negrete, Phys. Plasmas **13**, 082308 (2006).

[10] G.W. Hammett and F.W.Perkins, Phys. Rev. Lett., **64**, 25 (1990).

[11] I. Podlubny, Fractional Differential Equations (Academic Press, San Diego, 1999).

[12] R. Metzler and J. Klafter, Phys. Rep., **339**, 1, (2000).

[13] D. del-Castillo-Negrete, B.A. Carreras, and V. Lynch, Phys. Plasmas **11**, 3854 (2004).

[14] D. del-Castillo-Negrete, B.A. Carreras, and V.E. Lynch, Phys. Rev. Lett., **94**, 065003 (2005).

[15] R. Sanchez, B.A. Carreras, D.E. Newman, V.E. Lynch, and B.Ph. van Milligen, Phys. Rev. E. **71**, 011111 (2005).

[16] V. Lynch, B.A. Carreras, D. del-Castillo-Negrete, K.M. Ferreira-Mejias, and H.R. Hicks, J. Comput. Phys. **192**, 406–421 (2003).

[17] N. Tamura et al., Phys. Plasmas **12,** 110705 (2005).